Climatology of mesopause region nocturnal temperature, zonal wind, and sodium density observed by sodium lidar over Hefei, China (32°N, 117°E)

Tao Li[1*], Chao Ban[1,2*], Xin Fang[1], Jing Li[1], Zhaopeng Wu[1], Wuhu Feng[3,4], John M. C. Plane[3], Jianguang Xiong[5], Daniel R. Marsh[6], Michael J. Mills[6], and Xiankang Dou[1]

[1]CAS Key Laboratory of Geospace Environment, School of Earth and Space Sciences, University of Science and Technology of China, Hefei, Anhui, China

[2]Now at Institute of Atmospheric Physics, Chinese Academy of Sciences, Beijing, China[3]School of Chemistry, University of Leeds, Leeds, United Kingdom

[4]NCAS, School of Earth and Environment, University of Leeds, Leeds, United Kingdom

[5]Institute of Geology and Geophysics, Chinese Academy of Sciences, Beijing, China

[6]National Center for Atmospheric Research, Boulder, CO, USA

**To whom correspondence should be addressed: litao@ustc.edu.cn; banchao@mail.iap.ac.cn*

Abstract

The University of Science and Technology of China narrowband sodium temperature/wind lidar, located in Hefei, China (32°N, 117°E), has made routine nighttime measurements since January 2012. 154 nights (~1400 hours) of vertical profiles of temperature, sodium density, and zonal wind, and 83 nights (~800 hours) of vertical flux of gravity wave (GW) zonal momentum in the mesopause region (80-105 km) have been obtained during the period from 2012 to 2016. In temperature, it is most likely that the diurnal tide dominates below 100 km in spring, while the semidiurnal tide dominates above 100 km throughout the year. A clear semiannual variation in temperature is revealed near 90 km, in phase with the tropical mesospheric semiannual oscillation (MSAO). The variability of sodium density is positively correlated with temperature below 95 km, suggesting that in addition to dynamics, the chemistry also plays an important role in the formation of sodium atoms. The seasonal variability of sodium density observed by both lidar and satellite generally agrees well with a whole atmosphere model simulation using an updated meteoric input function which includes different cosmic dust sources. In zonal wind, the diurnal tide dominates in both spring and fall, while semidiurnal tide dominates in winter. The observed semiannual variation in zonal wind near 90 km is out-of-phase with that in temperature, consistent with the tropical MSAO. The lidar observations generally agree with satellite and meteor radar observations as well as

model simulations at similar latitude. The 50-70% of zonal momentum flux is induced by short-period (10 min – 2 hr) GWs. The large zonal momentum flux in summer and winter due to short-period GWs are clearly anti-correlated with eastward zonal wind maxima below 90 km, suggesting the filtering of short-period GWs by the SAO wind.

1. Introduction

The temperature and wind in the mesopause region (80-105 km) are key atmospheric parameters for studying the dynamics in this region. Ground-based instruments (e.g. lidars, radars), and space-borne instruments have been widely used to measure these key parameters over several decades (Vincent and Reid, 1983; She et al., 1998; Wu et al., 2008). Satellites can provide a near-global view of the mesopause region, but their local coverage is usually limited to two local times on the ascending and descending orbit. The lack of continuous coverage in local time makes it difficult to extract information on short period gravity wave (GW) perturbations from satellite data (Preusse et al., 2009). Ground-based meteor or medium frequency radars are capable of measuring mesopause wind in a continuous mode, but do not provide direct temperature measurements with sufficient accuracy and vertical resolution (Vincent and Reid, 1983). However, a narrowband sodium lidar is able to simultaneously measure mesopause region temperature and horizontal wind by utilizing the sodium high resolution spectrum (She et al., 1994; Arnold and She, 2003), which provides a unique opportunity to study GW perturbations and their breaking process in the mesopause region (Li et al., 2005; Li et al., 2007).

The long-term lidar observations have been used to study the seasonal variability of mesopause region temperature (She et al., 1998; Gardner et al., 2002; Xu et al., 2006; Friedman et al., 2007) and horizontal wind (Franke et al., 2005; Gardner et al., 2007), as well as sodium density (She et al., 2000; Gardner et al., 2005; Ejiri et al., 2010; Yi et al., 2009; Yuan et al., 2012), iron density (Yi et al., 2009; Lübken et al., 2011) and potassium density (Friedman et al., 2002; Plane et al., 2015). These datasets are extremely valuable to validate satellite results (Xu et al., 2006; Fan et al., 2007a; Dawkins et al., 2014) and improve general circulation models (Yuan et al., 2008; Feng et al., 2013; Marsh et al., 2013). When GWs break or dissipate in the mesopause region due to increased amplitudes or approaching critical level (where wave phase speed equal to horizontal background wind), they tend to deposit wave energy and momentum into the background flow, and further modify the temperature and wind near the breaking region (Lindzen et al., 1981; Liu and Hagan, 1998; Li et al., 2007). Therefore, measurements of the GW vertical flux of horizontal momentum and heat are critical for evaluating the GW contribution to the background state in this region, and their key roles in the dynamic coupling between lower and middle/upper atmosphere (Li et al.,

2013; 2016).

The vertical flux of horizontal momentum can be directly derived from the vertical wind perturbation and associated horizontal wind perturbation. To ensure accuracy of the GW momentum flux, the wind data must have high temporal and vertical resolutions with good precision and a long-time average (Kudeki and Franke, 1998; Thorsen et al., 2000). Several studies of lidar-observed GW momentum flux in the mesosphere/lower thermosphere (MLT) region have been carried out previously (Espy et al., 2004; Gardner and Liu, 2007; Acott et al., 2009).

In this paper, we present the seasonal variation of sodium density, temperature, zonal wind and GW zonal momentum flux observed by the University of Science and Technology of China (USTC) sodium temperature/wind lidar from January 2012 to December 2016 over Hefei, China (32°N, 117°E). This is the first time simultaneous observations of the seasonal variability of mesopause region temperature, zonal wind, and GW momentum flux by sodium lidar over the Eastern Asia region have been reported. We compare the lidar results with temperature observed by the Sounding of the Atmosphere Using Broadband Emission Radiometry (SABER) instrument onboard the Thermosphere–Ionosphere–Mesosphere Energetics and Dynamics (TIMED) satellite (Russell et al., 1999); zonal wind observed by a nearby meteor radar (Xiong et al., 2004); and sodium density observed by the Optical Spectrograph and InfraRed Imager System (OSIRIS) onboard the Odin satellite (Llewellyn et al., 2004). These measurements are then compared with simulations from the Whole Atmosphere Community Climate Model version 5 (WACCM) (Marsh et al., 2013; Mills et al., 2016; Feng et al., 2017), using an updated meteoric input function (MIF) for Na (Cárrillo-Sanchez et al., 2016). The instruments, datasets, and data analysis method are described in section 2, followed by the results of temperature and sodium density in section 3, and zonal wind and GW zonal momentum flux in section 4. A summary is provided in section 5.

2. Instruments, datasets and analysis method

The USTC sodium temperature/wind lidar, located on campus in Hefei, China (32°N, 117°E), utilizes a narrowband three-frequency design and can simultaneously observe sodium density, zonal wind and temperature in the mesopause region during nighttime clear sky

conditions (Li et al., 2012). The system was initially set up in October 2011 with two receiving telescopes (30-inch diameter) pointing eastward and northward 30° from zenith for measuring the zonal and meridional wind, respectively. The output laser beam is split into two beams, each aligned parallel to one telescope. Between December 2012 and May 2014 (total 83 nights), the two receiving telescopes were pointed to eastward and westward, each 15° from zenith. This dual-beam setup allows us to derive the GW zonal momentum flux as well as the zonal wind. Since June 2014, the westward telescope was pointed to vertical for measuring the vertical fluxes of heat and sodium atoms, and the eastward telescope to 30° from zenith for measuring zonal wind. Between January 2012 and December 2016, we obtained 154 nights (~1400 hours) of valid data, which is sufficient to study the seasonal variations of sodium density, temperature, zonal wind, and GW momentum flux (83 nights) in the mesopause region over Hefei. Figure 1 shows the number of nights with valid datasets in each month of the different years. It is clear that Hefei has more clear nights in fall and winter than in spring and summer.

The Wuhan (31°N, 114°E) meteor radar, located at ~300 km west of Hefei, has measured mesopause region horizontal wind since January 2002 (Xiong et al., 2004). The vertical and temporal resolutions of radar wind are 3 km and 2 hr, respectively. The SABER instrument onboard the TIMED satellite can measure the near-global vertical profile of temperature from the lower stratosphere to the lower thermosphere (Russell et al., 1999). The SABER temperature dataset used in this paper is Level2A version 2.0, which has a vertical resolution of 2 km and accuracies of ±1-2 K between 75 and 95 km, increasing to ±4 K at 100 km. The OSIRIS instrument onboard the Odin satellite measures solar-pumped Na resonance fluorescence from a sun-synchronous polar orbit (Llewellyn et al., 2004), and the datasets can be used to retrieve the global vertical profiles of sodium density between 75 and 110 km with a ~10% uncertainty for 2 km vertical resolution (Gumbel et al., 2007; Fan et al., 2007a).

To compare with lidar results, we also use the temperature, zonal wind, and sodium density simulated by the WACCM, a chemistry-climate model which extends from the Earth's surface to the lower thermosphere (~140 km) (Garcia et al., 2007; Marsh et al., 2013a). WACCM uses the framework from the fully coupled global climate model Community Earth System Model (CESM version 1, e.g., Hurrell et al., 2013). In this paper, we use a version of WACCM described in Mills et al. (2016), which includes all the detailed physical processes

as described in the Community Atmosphere Model, version 5 (CAM5) (Neale et al., 2012). The current configurations for WACCM are based on a finite volume dynamical core (Lin, 2004) for the tracer advection as well as a new surface topography data from Lauritzen et al. (2015). WACCM has the fully interactive chemistry described in Mills et al. (2016), and we have included the Na chemistry scheme listed in Plane et al. (2015) and Gomez Martin et al. (2015, 2017), with an updated meteoric input function (MIF) for Na (Cárrillo-Sanchez et al.,2016). The new MIF is calculated for the ablation of cosmic dust particles from Jupiter Family Comets (80% by mass), Asteroids (8%), and Long Period Comets (12%), and the injection rate of Na is about 8 times larger than that used in Marsh et al. (2013). The peak Na ablation rate from Cárrillo-Sanchez et al. (2016) occurs around 87 km, which is ~15 km lower than the MIF used in Marsh et al. (2013), which was based on meteor head radar measurements which were biased to the high velocity dust particles which mostly originate from Long Period Comets (Cárrillo-Sanchez et al., 2016). The absolute Na MIF used in this paper has been divided by a factor of 5 from that in Cárrillo-Sanchez et al. (2016), in order to match the observed Na layer density. This most likely reflects the fact that WACCM underestimates the rate of vertical transport of Na species in the MLT because sub-grid gravity waves are not resolved in the model (Huang et al., 2015). The horizontal resolution of WACCM is 1.9˚ latitude by 2.5˚ longitude. The vertical model layers and the vertical resolution are the same as Mills et al. (2017), which is 70 and ~3 km in the MLT region. Although the model can be nudged by a re-analysis dataset, in the current study we have used a "free-running" model simulation, which produces a satisfactory Na climatology in the model. We ran the model for year 2000 condition for 13 years.

The lidar raw photon counts are first analyzed to generate hourly mean vertical profiles of sodium density, temperature and line-of-sight (LOS) wind with 2 km vertical resolution for each direction. Before and after the dual-beam setup (eastward-westward) between December 2012 and May 2014, we assume that the hourly mean vertical wind is negligible and then derive the hourly mean zonal wind from the east channel LOS wind (eastward pointing at 30° from zenith). During the dual-beam setup, we derive the hourly mean zonal wind profiles by subtracting the hourly westward LOS wind from the eastward LOS wind and then dividing by $2\sin\theta$ (e.g. θ=20°) (Vincent and Reid,1983). The uncertainties of the hourly mean zonal wind and temperature typically range from ~1.0 m/s and ~0.5 K at 92 km (Na peak layer) to ~6 m/s

and ~5 K at 82 km and 103 km (the edge of Na layer), respectively. We then generate the nighttime hourly mean composite in each season.

Vincent and Reid (1983) presented a method utilizing the dual beam technique to derive vertical flux of GW horizontal momentum, when two beams are pointed at equal and opposite angle θ from the zenith. The zonal momentum flux $\overline{w'u'}$ is calculated as follows:

$$\overline{w'u'} = \frac{\overline{v^2(\theta,R)} - \overline{v^2(-\theta,R)}}{2\sin(2\theta)} \quad (1)$$

where $\overline{v^2(\theta,R)}$ and $\overline{v^2(-\theta,R)}$ are the square of the LOS wind perturbations in the east and west channels respectively, and θ is the zenith angle (e.g. 20°). To derive the momentum flux, we employed a similar procedure to that of Gardner and Liu (2007). Briefly, we first analyze lidar raw photon counts to generate the LOS wind with a temporal resolution of 5 min and a vertical resolution of 2 km. Data points with errors larger than 5 m/s were discarded during the quality check. We remove the linear trend and nightly mean from the LOS wind to form wind perturbations for each night. Data where the perturbation variances are smaller than the corresponding noise variances are also excluded. The seasonal mean vertical profile of perturbation variance is then obtained by averaging all available perturbation variances in that season. This process is done separately for each beam. Finally, the seasonal mean momentum flux is calculated using equation (1). In this way, the results only account for the GW perturbations with periods of 10 min-20 hr and vertical wavelengths of 4-30 km. We also apply a high-pass filter with cutoff at 2 hr on raw perturbations to examine the relative contribution of short-period GWs (10 min – 2 hr) to total momentum flux.

Since the meteor radar observed zonal wind is only available in 2013, we then calculate monthly mean with all available data for comparison. The SABER tracking points within ±5° latitude band (27-37°N) and longitude band (112-122°E) of the lidar site are selected first. We then discard the SABER temperature profiles that are outside of the lidar observation period. Finally, we average all available SABER temperature profiles within each month to form the monthly mean for comparison. A similar analysis method is used for the OSIRIS data. In the case of WACCM, the zonal mean data are first extracted at the coordinates of the lidar site and then the monthly mean profiles are generated in the same way as the lidar and radar profiles.

3. Temperature and sodium density

Figure 2 shows the hourly mean temperature composite in four different seasons. The temperatures below 95 km are generally warmer in fall and winter than in spring and summer, consistent with the mesospheric residual meridional circulation with upwelling in the summer hemisphere and downwelling in the winter hemisphere (Andrew et al., 1987; Smith, 2012). It is most likely that the diurnal tide with downward phase progression dominates below 100 km in spring, although we only have 10-12 hr data. However, the tidal feature is not clear below 95 km in other seasons. The temperature above 100 km in all seasons clearly exhibits two minima after dusk and before dawn and a maximum near midnight, suggesting dominance and persistence of the semidiurnal tide in this latitude region throughout the year.

The clear downward phase progression of diurnal and semidiurnal tides in mesopause temperature was previously observed by sodium lidar at the Starfire Optical Range (SOR), New Mexico (35°N, 107°W) (Chu et al., 2005). However, their observations suggest a clear dominance of diurnal in April and October and semidiurnal in January below 100 km, while we see a clear dominance of diurnal only in spring (March-May), and mixed features in other seasons. In addition, the midnight maximum above 100 km shown in our results is not observed over SOR. The SABER observations reveal a diurnal amplitude of ~2 K and ~8 K, and semidiurnal amplitude of ~7 K and ~12 K at 95km for the USTC and SOR lidar sites, respectively (Zhang et al., 2010). This significant longitudinal variability is likely due to nonlinear interactions between the migrating tide and non-immigrating tide (Forbes et al., 2003) and stationary planetary wave number 1 (Lieberman et al., 1991), respectively, and/or tidal/gravity waves interactions (Lindzen, 1981; Liu and Hagan, 1998; Li et al., 2007; 2009). The clear longitudinal variability of tides between two lidar sites could thus cause significant differences in the nocturnal climatology.

Figure 3 shows the monthly mean of the nightly mean temperature observed by lidar and SABER, and simulated by WACCM. All three figures show qualitative agreement in the general pattern, but difference in absolute values. The mesopause is clearly located near 100 km in winter and below 95 km in summer, indicating a two-level mesopause as previously observed at mid- and high latitudes (von Zahn et al., 1996; She et al., 1998). The lidar observed temperature above 95 km is ~10 K lower than SABER, likely due either to the low signal-to-noise ratio in the lidar return signals above 100 km (Li et al., 2012), or to a non-local

thermal equilibrium influence in the SABER analysis (Mertens et al., 2001). The lidar observed mesopause is also 5-10 K colder than that observed by SABER. The WACCM simulated temperature is clearly higher than both sets of observations at most altitudes and months. Yuan et al. (2008) showed a significant monthly mean mesopause region temperature difference between lidar observations and WACCM simulations over Fort Collins, CO (41°N, 105°W); their comparisons show that the WACCM-simulated winter mesopause is much warmer than measured by lidar, and the summer mesopause is ~3 km lower than lidar observations. Another interesting feature in all three figures is that we see a temperature maximum near ~90 km in March and April, and a second maximum in September and October, likely related to the mesospheric semiannual oscillation (MSAO) usually dominant in the equatorial middle atmosphere (Dunkerton, 1982; Burrage et al., 1996; Garcia et al., 1997).

Our measured monthly means of the nightly mean temperatures are also generally consistent with previously lidar observations at SOR (Gardner and Liu, 2007) and Fort Collins, CO (She et al., 1998; Yuan et al., 2008). However, the SOR lidar observations were ~10 K colder below 90 km in summer, and ~10 K warmer between 90 and 95 km in spring, suggesting significant differences between the two locations likely induced by the significant longitudinal variability of the diurnal tide (Zhang et al., 2010). The semiannual oscillation signature is evident over both Hefei and SOR between 90 and 95 km, but not over Fort Collins. The summer mesopause observed by lidar over Hefei is clearly higher than over the other two locations.

Figure 4 shows the hourly mean sodium density composite during the four different seasons. The density increases with local time during the night, with a peak height around 92 km. The peak density is overall much higher in fall and winter than in spring and summer, which is consistent with previous ground-based and satellite observations (She et al., 2000; Fan et al., 2007a; Fussen et al., 2010). Some peaks above 95 km in summer are likely induced by sporadic sodium layers (SSLs), which often occur in this season over Hefei (Dou et al., 2010). The seasonal mean sodium peak density in winter can reach 4000-4500 cm^{-3} after midnight. Figure 5 shows the monthly mean of nightly mean sodium density observed by (a) lidar and (b) Odin/OSIRIS, and simulated by (c) WACCM. Both observations agree well in seasonal pattern and absolute sodium density, and are also consistent with the WACCM

model simulation. The elevated peak height and enhanced density in summer observed by lidar is likely due to increased SSL events in summer over Hefei, which is neither frequently observed by Odin/OSIRIS nor simulated by WACCM. The Odin/OSIRIS did observe SSLs over China (Fan et al., 2007b), but probably less frequently at 0600 and 1800 local time than at midnight. The observed sodium density over Hefei is quite consistent with previous narrowband lidar observations over Fort Collins, CO (She et al., 2000) and Urbana, IL (States and Gardner, 1998), but ~1.5 times higher than previous broadband sodium lidar observations over the nearby city of Wuhan, China (Yi et al., 2009).

The variability of sodium density is clearly correlated with the temperature variability shown in Figure 2. This is further demonstrated in Figure 6, where the correlation coefficient between the composite temperature and relative sodium density perturbations is plotted using lidar measurements (left) and the WACCM simulation (right). The temporal resolution for both lidar and WACCM is 1 hr. We also examined the correlation in the four different seasons and found no significant differences. The lidar observations are clearly consistent with the WACCM simulation, and both results suggest a positive correlation with coefficient of 0.5-0.8 between 80-90 km, but a negative correlation with coefficient of less than ~-0.4 above 96 km for lidar and 100 km for WACCM, consistent with lidar observations at Urbana (40N) (Plane *et al*., 1999) and in the Arctic (Collins and Smith, 2004). However, our lidar observations above 95 km are not consistent with the recent sodium lidar observations at ALOMAR, which showed a positive correlation with temperature above this altitude (Dunker et al., 2015). This difference may be related to energetic particle precipitation at high latitudes, but the detailed mechanism is beyond scope of this paper.

Our lidar observations suggest that the main chemistry below 95 km is likely dominated by neutral sodium chemistry, which essentially involves the partitioning of the metal between atoms and the main reservoir $NaHCO_3$; the significant activation energy of the reaction $NaHCO_3 + H$ drives the balance towards Na at higher temperatures. In contrast, above 95 km the source of atomic Na is from Na^+, which involves formation of cluster ions that then undergo dissociative recombination with electrons; the formation of cluster ions is favored at lower temperatures, hence the negative correlation coefficient between and Na and temperature on the topside of the Na layer (Plane et al., 2015).

4. Zonal wind and gravity wave momentum flux

Figure 7 shows the hourly mean zonal wind composite in 4 different seasons. We see strong tidal oscillations with downward phase progression in all seasons, much clearer than those in temperature (Figure 2). The diurnal tide with vertical wavelength of ~ 20 km dominates in both spring and fall, while the semidiurnal tide with vertical wavelength of 30-40 km dominates in winter. In spring, the diurnal tide in temperature (Figure 2a) leads that in zonal wind by ~4hr between 90 and 95 km, consistent with earlier mid-latitude observations (Yuan et al., 2006). There is a strong wave oscillation signature with a period of ~8hr and amplitude of ~20 m/s that dominates in summer, possibly related to the terdiurnal tide. Previous observations by the nearby Wuhan meteor radar show that the diurnal amplitude near 90 km during equinox is ~ 30 m/s, with a semidiurnal amplitude of ~10 m/s (Xiong et al., 2004; Zhao et al., 2005). The comparable amplitude (~10 m/s) of diurnal and semidiurnal in winter is also revealed by these radar observations, with which our observations are generally consistent.

We show in Figure 8 the monthly mean of the nightly mean zonal wind observed by (a) lidar, (b) Wuhan meteor radar, and (c) simulated by WACCM. The radar observed zonal wind is only available in 2013 for comparison. The general pattern of the lidar observed zonal winds agrees well with the radar winds, but are 5-10 m/s stronger. This is likely due to the different vertical and temporal resolutions, signal-to-noise ratio, and the mesurement methods, as well as the different locations. The lidar results exhibit a semiannual variation near 90 km with minima in March and August/September, and one maximum in May/June, clearly out-of-phase with the temperature semiannual variation (Figure 3a). The lidar observed semiannual variation in both wind and temperature is consistent with the tropical MSAO previously observed by satellites (Garcia et al., 1997), and simulated by WACCM (Richter and Garcia, 2006). The lidar and radar observations agree with the WACCM simulation below 90 km in both pattern and magnitude, while disagreeing above. Interestingly, a recent comparision between lidar measurements over Fort Collins, CO and several general circulation models also reveals significant differences (Yuan et al., 2008).

The USTC lidar telescopes were pointed 15° from zenith in eastward and westward directions between December 2012 and May 2014. This setup allows us to derive the vertical flux of GW zonal momentum. A total of 83 nights of GW momentum flux measurements

were obtained with 21, 12, 23, and 27 nights in spring, summer, fall, and winter respectively. Figure 9 shows vertical profiles of the seasonal mean GW zonal momentum flux for period 10min – 16hr (blue) and 10min – 2hr (green), and zonal wind (red) in (a) spring, (b) summer, (c) fall, and (d) winter. The zonal momentum flux is mostly eastward in spring, positively correlated with the eastward zonal wind. However, the zonal momentum flux is mostly westward in other seasons, clearly anti-correlated with the eastward zonal wind, suggesting zonal wind filtering of GWs below 80 km. It is also clear that the zonal momentum flux induced by short-period (10 min – 2 hr) GWs clearly dominates total momentum flux in all seasons except summer.

The seasonal variation of zonal momentum flux is consistent with previous sodium lidar observation at SOR, NM (Gardner and Liu, 2007). However, MU radar observations near Kyoto, Japan (35°N, 136°E) shows a clear eastward flux in summer and westward flux in winter between 65 and 85 km (Tsuda et al., 1990). MF radar observations in Adelaide, Australia (35°S, 138°E) suggest an eastward flux of ~3 m^2/s^2 in winter (Reid and Vincent, 1987). We note here that part of the differences between our lidar results and other published work is likely due to different vertical and temporal resolutions and thus sensitivity to different portions of the GW spectrum. Table 1 compares the GW zonal momentum flux measured at different mid-latitude lidar and radar stations. The results from other locations are estimated from the following studies: Gardner and Liu (2007) for the SOR lidar results; Acott et al. (2009) for the Fort Collins, CO lidar results; and Tsuda et al. (1990) for the Japan MU radar results. This comparison demonstrates that all observations report a clear westward GW zonal momentum flux in winter. In spring, both the USTC and SOR lidars observed an eastward momentum flux of 1.4-2 m^2/s^2.

The short-period (10 min – 2 hr) GWs clearly contribute 50%-70% of the total momentum flux, consistent with previously medium frequency (MF) radar observations (Fritts and Vincent, 1987). The large westward momentum fluxes of -0.9 and -0.6 m^2/s^2 for short-period GWs in summer and winter respectively are clearly anti-correlated with eastward zonal wind maxima below 90 km (Figure 8a), suggesting the filtering of short-period GWs by the SAO wind. However, this SAO variation is not clear in the total momentum flux. For the annual mean, our lidar result is clearly smaller than the SOR lidar result, mainly due to significant difference in summer. Our results also show that the annual mean zonal wind

345 averaged between 87-95 km is ~10 m/s eastward, and anti-correlated with the westward
346 momentum flux of ~-0.15 m^2/s^2 induced by short-period GWs. This anti-correlation suggests
347 that the GW momentum flux observed in the mesopause region is generally consistent with
348 the wind filtering theory proposed by Lindzen (1981), and adopted by general circulation
349 models (e.g. Richter et al., 2010).
350
351 **5. Summary**
352 Between 2012 and 2016, the USTC sodium temperature/wind lidar observed mesopause
353 region nighttime temperature, zonal wind, and sodium density over 150 nights, and the
354 vertical flux of zonal momentum during 83 nights. The seasonal nighttime hourly composites
355 of temperature and zonal wind show clear diurnal and/or semidiurnal tidal signatures. In
356 temperature, the diurnal tide with clear downward phase progression dominates only in spring,
357 while the semidiurnal tide dominates above 100 km throughout the year. In zonal wind, the
358 diurnal tide with vertical wavelength of ~ 20 km dominates in both spring and fall, while the
359 semidiurnal tide with vertical wavelength of 30-40 km dominates in winter. Between 90 and
360 95 km, the diurnal tide in temperature in spring leads that in zonal wind by ~4 hr, consistent
361 with previous observations and model simulations. The monthly mean results show a
362 signature of semiannual variation in both temperature and zonal wind near 90 km but with
363 clear out-of-phase feature, consistent with the tropical MSAO. Comparison of the USTC lidar
364 results with observations by satellite and meteor radar, and simulated by WACCM show
365 generally good agreement, although there are some differences among them, with pronounced
366 disagreement between the observed zonal wind and the model above 90 km.
367 The seasonal mean of zonal momentum flux is mostly westward in summer, fall and
368 winter, clearly anti-correlated with the eastward zonal wind, which suggests zonal wind
369 filtering of GWs below 80 km. However, during spring the zonal momentum flux is mostly
370 eastward, positively correlated with the eastward zonal wind. The short-period GWs clearly
371 contribute 50%-70% of total momentum flux averaged over 87-95 km. The large westward
372 momentum fluxes in summer and winter for short-period GWs are clearly anti-correlated with
373 eastward zonal wind maxima below 90 km (Figure 8a), suggesting the filtering of
374 short-period GWs by the SAO wind. The annual mean flux averaged over 87-95 km is ~-0.15
375 m^2/s^2 (westward) induced by the short-period GWs, anti-correlated with the zonal wind of

~10 m/s (eastward), suggesting that the GW momentum flux observed in the mesopause region is generally consistent with the wind filtering theory.

The sodium density increases with local time during the night, with a peak height near 92 km. The peak density is overall much higher in fall and winter than in spring and summer. The seasonal mean sodium peak density in winter can reach 4000-4500 cm^{-3} after mid-night. The variability of sodium density is positively correlated with temperature variability, suggesting that chemistry plays a dominant role in the formation of sodium atoms in the mesopause region below 95 km. The lidar observations agree well with Odin/OSRIS satellite observations in both seasonal pattern and absolute monthly mean sodium density, consistent with WACCM simulations using a new Na meteoric input function.

Acknowledgments

The work described in this paper was carried out at the University of Science and Technology of China (USTC), under support of the National Natural Science Foundation of China grant 41674149 and the Open Research Project of Large Research Infrastructures of CAS - "Study on the interaction between low/mid-latitude atmosphere and ionosphere based on the Chinese Meridian Project. WF and JMCP were supported by the European Research Council (project 291332-CODITA). The National Center for Atmospheric Research (NCAR) is sponsored by the National Science Foundation. We thank Chengyun Yang, Shengyang Gu, Xianyu Wang, Yetao Cen, Feng Li, and Huazhi Ge for help to take lidar data. TL would like to thank Alan Liu for helpful discussion. The SD-WACCM model was obtained from the NCAR and run at the University of Leeds and is available for contacting the co-authors FW or JMCP. We would like to thank Francis Vitt at NCAR for the WACCM model support. The SABER data is downloaded from http://saber.gats-inc.com/. We thank Richard Collins and another anonymous reviewer for their constructive comments.

401 **Reference:**

402 Acott, P. E., C. Y. She, D. A. Krueger, Z. A. Yan, T. Yuan, J. Yue, and S. Harrell (2011),
403 Observed nocturnal gravity wave variances and zonal momentum flux in mid-latitude
404 mesopause region over Fort Collins, Colorado, USA, J. Atmos. Sol. Terr. Phys., 73(4),
405 449–456, doi:10.1016/j.jastp.2010.10.016.

406 Andrews, D. G., J. R. Holton, and C. B. Leovy (1987), Middle Atmosphere Dynamics, 489
407 pp., Elsevier, New York.

408 Arnold, K., and C. She (2003), Metal fluorescence lidar (light detection and ranging) and the
409 middle atmosphere, Contemporary Physics, 44(1), 35–49,
410 doi:10.1080/0010751021000019157.

411 Burrage, M. D., R. A. Vincent, H. G. Mayr, W. R. Skinner, N. F. Arnold, and P. B. Hays
412 (1996), Long-term variability in the equatorial middle atmosphere zonal wind, J.
413 Geophys. Res., 101(D), 12–, doi:10.1029/96JD00575.

414 Carrillo-Sánchez, J. D., D. Nesvorný, P. Pokorný, D. Janches, and J. M. C. Plane (2016),
415 Sources of cosmic dust in the Earth's atmosphere, Geophys. Res. Lett., 43, 11,979–
416 11,986, doi:10.1002/ 2016GL071697.

417 Chu, X., C. S. Gardner, and S. J. Franke (2005), Nocturnal thermal structure of the
418 mesosphere and lower thermosphere region at Maui, Hawaii (20.7°N), and Starfire
419 Optical Range, New Mexico (35°N), J. Geophys. Res., 110(D), D09S03,
420 doi:10.1029/2004JD004891.

421 Collins, R. L. and Smith, R. W.: Evidence of damping and overturning of gravity waves in the
422 Arctic mesosphere: Na lidar and OH temperature observations, J. Atmos. Sol. Terr. Phys.,
423 66(10), 867–879, doi:10.1016/j.jastp.2004.01.038, 2004.

424 Dou, X. - K., X. - H. Xue, T. Li, T. - D. Chen, C. Chen, and S. - C. Qiu (2010), Possible
425 relations between meteors, enhanced electron density layers, and sporadic sodium layers,
426 J. Geophys. Res., 115, A06311, doi:10.1029/2009JA014575.

427 Dawkins, E. C. M., J. M. C. Plane, M. P. Chipperfield, W. Feng, J. Gumbel, J. Hedin, J.
428 Hoffner, and J. S. Friedman (2014): First global observations of the mesospheric
429 potassium layer, Geophys. Res. Lett., 41, 5653-5661.

430 Dunker, T., U.-P. Hoppe, W. Feng, J. M. C. Plane, and D. R. Marsh (2015), Mesospheric
431 temperatures and sodium properties measured with the ALOMAR Na lidar compared

with WACCM, J. Atmos. Sol. Terr. Phys., 127, 111–119, doi:10.1016/j.jastp.2015.01.003.

Dunkerton, T. J. (1982), Theory of the Mesopause Semiannual Oscillation, J. Atmos. Sci., 39(12), 2681–2690, doi:10.1175/1520-0469(1982)039<2681:TOTMSO>2.0.CO;2.

Ejiri, M. K., T. Nakamura, and T. D. Kawahara (2010), Seasonal variation of nocturnal temperature and sodium density in the mesopause region observed by a resonance scatter lidar over Uji, Japan, J. Geophys. Res., 115, D18126, doi:10.1029/2009JD013799.

Espy, P. J., G. O. L. Jones, G. R. Swenson, J. Tang, and M. J. Taylor (2004), Seasonal variations of the gravity wave momentum flux in the Antarctic mesosphere and lower thermosphere, J. Geophys. Res., 109, D23109, doi:10.1029/2003JD004446.

Fan, Z. Y., J. M. C. Plane, J. Gumbel, J. Stegman, and E. J. Llewellyn (2007a), Satellite measurements of the global mesospheric sodium layer, Atmospheric Chemistry and Physics, 7, 4107-4115.

Fan, Z. Y., J. M. C. Plane, and J. Gumbel (2007b), On the global distribution of sporadic sodium layers, *Geophysical Research Letters*, *34*, Article number L15808

Feng, W., Marsh, D. R., Chipperfield, M. P., Janches, D., Hoffner, J. Yi, F., and Plane, J. M. C. (2013): A global atmospheric model of meteoric iron, *Journal of Geophysical Research*, *118*, 9456–9474.

Feng, W., B. Kaifler, D. R. Marsh, J. Höffner, U.-P. Hoppe, B. P. Williams, and J. M. C. Plane (2017), Impacts of a sudden stratospheric warming on the mesospheric metal layers, J. Atmos. Sol. Terr. Phys., 1–10, doi:10.1016/j.jastp.2017.02.004.

Forbes, J. M., X. Zhang, W. Ward, and E. Talaat (2003), Nonmigrating diurnal tides in the thermosphere, J. Geophys. Res., 108(A1), 1033, doi:10.1029/2002JA009262.

Franke, S. J., X. Chu, A. Z. Liu, and W. K. Hocking (2005), Comparison of meteor radar and Na Doppler lidar measurements of winds in the mesopause region above Maui, Hawaii, J. Geophys. Res., 110, D09S02, doi:10.1029/2003JD004486.

Friedman, J. S., S. C. Collins, R. Delgado, and P. A. Castleberg (2002), Mesospheric potassium layer over the Arecibo Observatory, 18.3°N 66.75°W, Geophys. Res. Lett., 29(5), 1071, doi:10.1029/2001GL013542.

Friedman, J.S., Chu,X. (2007) Nocturnal temperature structure in the mesopause region over the Arecibo Observatory (18.351N, 66.751W): seasonal variations. J. Geophys. Res.,

112(D11), D14107.

Fritts, D. and Vincent, R.: Mesospheric Momentum Flux Studies at Adelaide, Australia: Observations and a Gravity Wave-Tidal Interaction Model, Journal of the Atmospheric Sciences, 44(3), 605–619, 1987.

Fussen, D., Vanhellemont, F., Tétard, C., Mateshvili, N., Dekemper, E., Loodts, N., et al. (2010). A global climatology of the mesospheric sodium layer from GOMOS data during the 2002-2008 period. Atmospheric Chemistry and Physics, 10(1), 9225–9236, doi:10.5194/acp-10-9225-2010.

Garcia, R. R., T. J. Dunkerton, R. S. Lieberman, and R. A. Vincent (1997), Climatology of the semiannual oscillation of the tropical middle atmosphere, J. Geophys. Res., 102(D), 26–, doi:10.1029/97JD00207.

Garcia, R. R., D. Marsh, D. E. Kinnison, B. Boville, and F. Sassi, Simulations of secular trends in the middle atmosphere, 1950-2003, J. Geophys. Res., 112, D09301, doi:10.1029/2006JD007485, 2007.

Gardner, C. S., Y. Zhao, and A. Z. Liu (2002), Atmospheric stability and gravity wave dissipation in the mesopause region, J. Atmos. Sol. Terr. Phys., 64, 923– 929, doi:10.1016/S1364-6826(1002)00047-00040.

Gardner, C. S., J. M. C. Plane, W. Pan, T. Vondra, B. J. Murray, and X. Chu (2005), Seasonal variations of the Na and Fe layers at the South Pole and their implications for the chemistry and general circulation of the polar mesosphere, J. Geophys. Res., 110, D10302, doi:10.1029/2004JD005670.

Gardner, C. S., and Liu A. Z. (2007), Seasonal variations of the vertical fluxes of heat and horizontal momentum in the mesopause region at Starfire Optical Range, New Mexico, J. Geophys. Res., 112, D09113, doi:10.1029/2005JD006179.

Gómez Martín, J.C., et al., Reaction Kinetics of Meteoric Sodium Reservoirs in the Upper Atmosphere, J. Phys. Chem. A, 2015, DOI: 10.1021/acs.jpca.5b00622

Gómez Martín, J.C., et al., The Reaction Between Sodium Hydroxide and Atomic Hydrogen in Atmospheric and Flame Chemistry, J. Phys. Chem. A, 2017, doi:10.1021/acs.jpca.7b07808.

Huang, W.; Chu, X. Z.; Gardner, C. S.; Carrillo-Sanchez, J. D.; Feng, W.; Plane, J. M. C.; Nesvorny, D. (2015): Measurements of the vertical fluxes of atomic Fe and Na at the

494 mesopause: Implications for the velocity of cosmic dust entering the atmosphere,
495 *Geophysical Research Letters*, *42*, 169-175.
496 Hurrell, J. W., Holland, M. M., Gent, P. R., Ghan, S., Kay, J. E., Kushner, P. J., Lamarque, J.
497 F., Large, W. G., Lawrence, D., Lindsay, K., Lipscomb, W. H., Long, M. C., Mahowald,
498 N., Marsh, D. R., Neale, R. B., Rasch, P., Vavrus, S., Vertenstein, M., Bader, D., Collins,
499 W. D., Hack, J. J., Kiehl, J. and Marshall, S.: The Community Earth System Model: A
500 Framework for Collaborative Research, Bulletin of the American Meteorological Society,
501 94(9), 1339–1360, doi:10.1175/BAMS-D-12-00121.1, 2013.
502 Kudeki, E., and S. J. Franke (1998), Statistics of momentum flux estimation, J. Atmos. Sol.
503 Terr. Phys., 60, 1549– 1553.
504 Lauritzen, P. H., Bacmeister, J. T., Callaghan, P. F., and Taylor, M. A.: NCAR global model
505 topography generation software for unstructured grids, Geosci. Model Dev., 8, 1-12,
506 doi:10.5194/gmd-8-1-2015, 2015
507 Li, T., C. She, B. Williams, T. Yuan, R. Collins, L. Kieffaber, and A. Peterson (2005),
508 Concurrent OH imager and sodium temperature/wind lidar observation of localized
509 ripples over northern Colorado, J. Geophys. Res., 114, D06106,
510 doi:10.1029/2008JD011089.
511 Li, T., C. She, H. Liu, and M. Montgomery (2007), Evidence of a gravity wave breaking
512 event and the estimation of the wave characteristics from sodium lidar observation over
513 Fort Collins, CO (41°N, 105°W), Geophys. Res. Lett., 34, L05815,
514 doi:10.1029/2006GL028988.
515 Li, T., C.-Y. She, H.-L. Liu, J. Yue, T. Nakamura, D. A. Krueger, Q. Wu, X. Dou, and S.
516 Wang (2009), Observation of local tidal variability and instability, along with dissipation
517 of diurnal tidal harmonics in the mesopause region over Fort Collins, Colorado (41°N,
518 105°W), J. Geophys. Res., 114, D06106, doi:10.1029/2008JD011089.
519 Li, T., X. Fang, W. Liu, S. Y. Gu, and X. K. Dou (2012), Narrowband sodium lidar for the
520 measurements of mesopause region temperature and wind, Appl. Optics, 51(22),
521 5401-5411, doi:10.1364/ao.51.005401.
522 Li, T., N. Calvo, J. Yue, X. Dou, J. M. Russell III, M. G. Mlynczak, C.-Y. She, and X. Xue
523 (2013), Influence of El Niño-Southern Oscillation in the mesosphere, Geophys. Res. Lett.,
524 40(12), 3292–3296, doi:10.1002/grl.50598.

525 Li, T., N. Clavo, J. Yue, J. Russel III, A. Smith, M. Mlynczak, A. Chandran, X. Dou, and A.
526 Liu (2016), Southern Hemisphere summer mesopause responses to El Niño–Southern
527 Oscillation, J. Clim., 29, 6319–6328, doi:10.1175/JCLI-D-15-0816.1.
528 Lieberman, R. S. (1991), Nonmigrating diurnal tides in the equatorial middle atmosphere, J.
529 Atmos. Sci., 48, 1112–1123.
530 Lin, S.–J., A "vertically-Lagrangian" finite-volume dynamical core for global atmospheric
531 models, Mon. Wea. Rev., 132, 2293-2307, 2004.
532 Lindzen, R. S. (1981), Turbulence and stress owing to gravity-wave and tidal breakdown, J.
533 Geophys. Res., 86(NC10), 9707-9714, doi:10.1029/JC086iC10p09707.
534 Liu, H. L., and M. E. Hagan (1998), Local heating/cooling of the mesosphere due to gravity
535 wave and tidal coupling, Geophys. Res. Lett., 25(15), 2941-2944,
536 doi:10.1029/98gl02153.
537 Lübken F, Höffner J, Viehl TP, Kaifler B, Morris RJ (2011), First measurements of thermal
538 tides in the summer mesopause region at Antarctic latitudes. Geophys. Res. Lett., 38,
539 L24806. doi:10.1029/ 2011GL0500458.
540 Llewellyn, E. J., et al. (2004). The OSIRIS instrument on the Odin spacecraft, Can. J. Phys.,
541 82, 411–422.
542 Marsh, D. R., M. J. Mills, D. E. Kinnison, J.-F. Lamarque, N. Calvo, and L. M. Polvani
543 (2013a), Climate Change from 1850 to 2005 Simulated in CESM1(WACCM), Journal of
544 Climate, 26(19), 7372–7391, doi:10.1175/JCLI-D-12-00558.1.
545 Marsh, D. R., Janches, D., Feng, W., and Plane, J. M. C. (2013b). A global model of meteoric
546 sodium. J. Geophys. Res., 118(1), 11,442–11,452, doi:10.1002/jgrd.50870.
547 Mertens, C. J., M. G. Mlynczak, M. López-Puertas, P. P. Wintersteiner, R. H. Picard, J. R.
548 Winick, L. L. Gordley, and J. M. I. Russell (2001), Retrieval of mesospheric and lower
549 thermospheric kinetic temperature from measurements of CO2 15 μm Earth Limb
550 Emission under non-LTE conditions, Geophys. Res. Lett., 28(7), 1391–1394,
551 doi:10.1029/2000GL012189.
552 Mills, M. J. et al. (2016), Global volcanic aerosol properties derived from emissions,
553 1990-2014, using CESM1(WACCM), J Geophys Res-Atmos, 121(5), 2332–2348,
554 doi:10.1002/2015jd024290.
555 Mills, M. J., Richter, J. H., Tilmes, S., Kravitz, B., MacMartin, D. G., Glanville, A. A.,

556 Tribbia, J. J., Lamarque, J.-F., Vitt, F., Schmidt, A., Gettelman, A., Hannay, C.,
557 Bacmeister, J. T. and Kinnison, D. E.: Radiative and Chemical Response to Interactive
558 Stratospheric Sulfate Aerosols in Fully Coupled CESM1(WACCM), Journal of
559 Geophysical Research-Atmospheres, 6(3), 541, doi:10.1002/2017JD027006, 2017.
560 Neale, R.B., C.C. Chen, A. Gettelman and Coauthors, 2012: Description of the NCAR
561 Community Atmosphere Model (CAM 5.0). NCAR Tech. Note NCAR-TN-486+STR,
562 274 pp.
563 Plane, J. M. C., C. S. Gardner, J. Yu, C.Y. She, R. R. Garcia and H. C. Pumphrey (1999), The
564 Mesospheric Na layer at 40^{o}N: Modelling and Observations. *Journal of Geophysical*
565 *Research*, *104*, 3773-3788.
566 Plane, J. M. C., W. Feng, and E. C. M. Dawkins (2015), The Mesosphere and Metals:
567 Chemistry and Changes, Chem. Rev., 115(10), 4497–4541, doi:10.1021/cr500501m.
568 Preusse, P., S. D. Eckermann, M. Ern, J. Oberheide, R. H. Picard, R. G. Roble, M. Riese, J. M.
569 Russell, and M. G. Mlynczak (2009), Global ray tracing simulations of the SABER
570 gravity wave climatology, J. Geophys. Res., 114(D), D08126,
571 doi:10.1029/2008JD011214.
572 Reid, I. M.: Measurements of mesospheric gravity wave momentum fluxes and mean flow
573 accelerations at Adelaide, Australia, Jourmd of Atmospheric and Terresfrial Physrcs, 1–
574 18, 1987.
575 Richter, J. H., F. Sassi, and R. R. Garcia (2010), Toward a Physically Based Gravity Wave
576 Source Parameterization in a General Circulation Model, Journal of the Atmospheric
577 Sciences, 67, 136, doi:10.1175/2009JAS3112.1.
578 Russell, J. M., III, M. G. Mlynczak, L. L. Gordley, J. Tansock, and R. Esplin (1999), An
579 overview of the SABER experiment and preliminary calibration results, Proc. SPIE, 3756,
580 277– 288.
581 She, C. Y., and J. R. Yu (1994), Simultaneous three-frequency Na lidar measurements of
582 radial wind and temperature in the mesopause region, Geophys. Res. Lett., 21(1), 1771–
583 1774, doi:10.1029/94GL01417.
584 She, C.Y., S. W. Thiel, D. A. Krueger (1998), Observed Episodic Warming at 86 and 100 km
585 Between 1990 and 1997: Effects of Mount Pinatubo Eruption, Geophys. Res. Lett., 25(4),
586 497-500, doi: 10.1029/98GL00178

587 She, C. Y. (2000), Eight-year climatology of nocturnal temperature and sodium density in the
588 mesopause region (80 to 105 km) over Fort Collins, Co (41°N, 105°W), Geophys. Res.
589 Lett., 27(20), 3289-3292, doi: 10.1029/2000GL003825.
590 Smith, A. K. (2012), Global Dynamics of the MLT, Surv. Geophys., 33(6), 1177–1230,
591 doi:10.1007/s10712-012-9196-9.
592 States, R. J., & Gardner, C. S. (1999). Structure of the mesospheric Na layer at 40°N latitude:
593 Seasonal and diurnal variations. J. Geophys. Res., 104(D), 11,783-11,798. doi:
594 10.1029/1999JD900002.
595 Thorsen, D., S. J. Franke, and E. Kudeki (2000), Statistics of momentum flux estimation
596 using the dual coplanar beam technique, Geophys. Res. Lett., 27, 3193–3196.
597 Tsuda, T., Y. Murayama, and M. Yamamoto (1990), Seasonal variation of momentum flux in
598 the mesosphere observed with the MU radar, Geophys. Res. Lett., 17, 725–728.
599 Vincent, R. A., and I. M. Reid (1983), HF doppler measurements of mesospheric
600 gravity-wave momentum fluxs, J. Atmos. Sci., 40(5), 1321-1333,
601 doi:10.1175/1520-0469(1983)040<1321:hdmomg>2.0.co;2.
602 Wu, Q., D. A. Ortland, T. L. Killeen, R. G. Roble, M. E. Hagan, H. L. Liu, S. C. Solomon, J.
603 Xu, W. R. Skinner, and R. J. Niciejewski (2008), Global distribution and interannual
604 variations of mesospheric and lower thermospheric neutral wind diurnal tide: 1.
605 Migrating tide, J. Geophys. Res., 113(A), A05308, doi:10.1029/2007JA012542.
606 Xiong, J. G., W. Wan, B. Ning, and L. Liu (2004), First results of the tidal structure in the
607 MLT revealed by Wuhan Meteor Radar (30 degrees 40 ' N, 114 degrees 30 ' E), J. Atmos.
608 Sol.-Terr. Phys., 66(6-9), 675-682, doi:10.1016/j.jastp.2004.01.018.
609 Xu, Jiyao, She, C. Y., Yuan Wei, Mertens Chris, Mlynczak Marty, Russell, James (2006),
610 Comparison between the temperature measurements by TIMED/SABER and lidar in the
611 midlatitude, J. Geophys. Res., 11(A10), doi:10.1029/2005JA011439
612 Yi, F., C. Yu, S. Zhang, X. Yue, Y. He, C. Huang, Y. Zhang, and K. Huang (2009), Seasonal
613 variations of the nocturnal mesospheric Na and Fe layers at 30°N, J. Geophys. Res., 114,
614 D01301, doi:10.1029/2008JD010344.
615 Yuan, T., et al. (2006), Seasonal variation of diurnal perturbations in mesopause region
616 temperature, zonal, and meridional winds above Fort Collins, Colorado (40.6°N, 105°W),
617 J. Geophys. Res., 111, D06103, doi:10.1029/2004JD005486.

618 Yuan, T., She, C. Y., Kawahara Takuya D., Krueger, D. A. (2012), Seasonal variations of
619 midlatitude mesospheric Na layer and their tidal period perturbations based on full
620 diurnal cycle Na lidar observations of 2002–2008, J. Geophys. Res., 117(D11),
621 doi:10.1029/2011JD017031.
622 Zahn, von, U., J. Hoffner, V. Eska, and M. Alpers (1996), The mesopause altitude: Only two
623 distinctive levels worldwide? Geophys. Res. Lett., 23(2), 3231–3234,
624 doi:10.1029/96GL03041.
625 Zhang, X., J. M. Forbes, and M. E. Hagan (2010), Longitudinal variation of tides in the MLT
626 region: 1. Tides driven by tropospheric net radiative heating, J. Geophys. Res., 115,
627 A06316, doi:10.1029/2009JA014897.
628 Zhao, G., L. Liu, W. Wan, B. Ning, and J. Xiong (2005), Seasonal behavior of meteor radar
629 winds over Wuhan, Earth Planets and Space, 57(1), 61–70, doi:10.1186/BF03351806.

630 **Table 1.** Comparison of the GW zonal momentum flux (m^2/s^2) measured at different middle
631 latitude lidar and radar stations.

Stations	Altitude/filter	Annual	Spring	Summer	Fall	Winter
USTC lidar (32°N, 117°E)	87 – 95 km 10min – 16hr	-0.08	1.4	-0.2	-0.3	-0.9
	87 – 95 km 10min – 2hr	-0.15	0.8	-0.9	-0.16	-0.6
SOR lidar (35°N, 107°W)	85 – 100 km 3min – 14hr	-1.2	~2	1.8	N/A	-1.7
CSU lidar (41°N, 105°W)	85 – 95 km 6min – 4hr	N/A	~0.1	N/A	~0.1	-0.7
MU Radar (35°N, 136°E)	65 – 85km 5min – 2 hr	N/A	~0	2.0	~0	-1.5

632

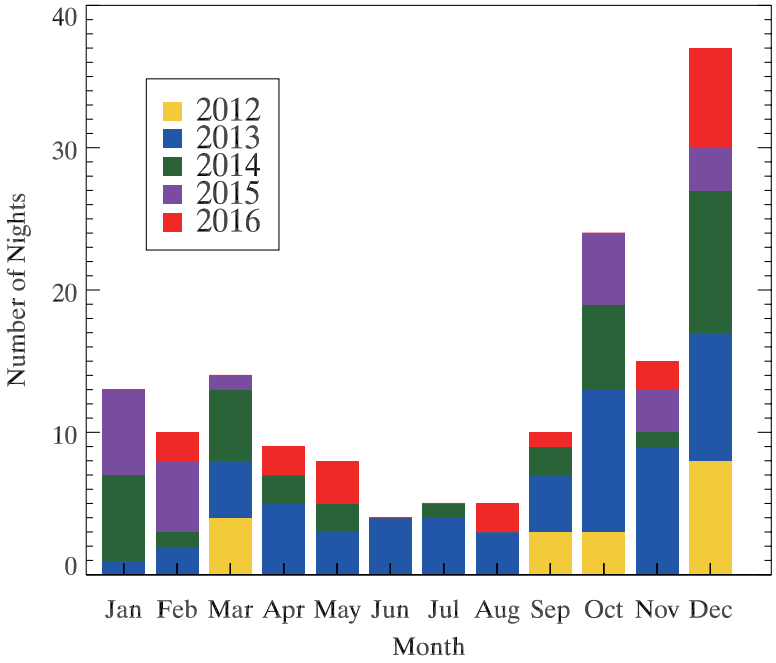

633

634 **Figure 1.** Histogram of number of nights with valid data observed by the USTC sodium lidar.

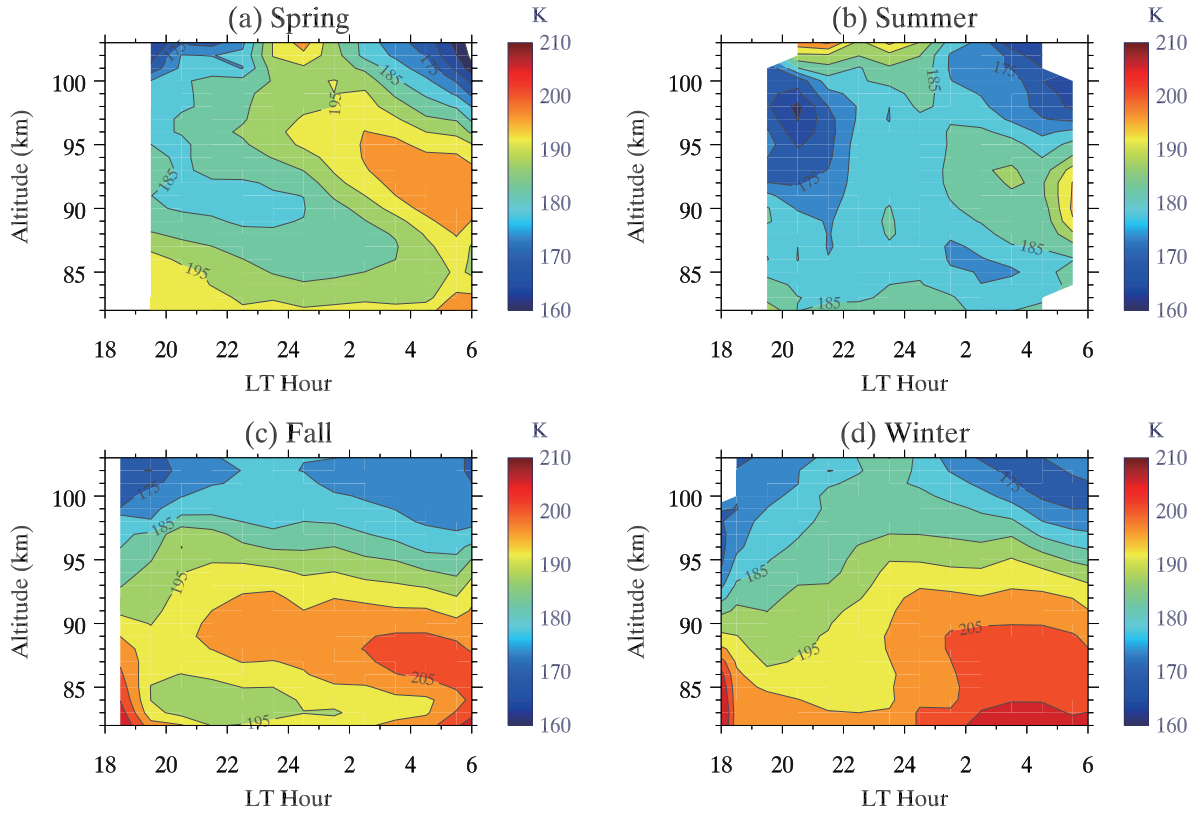

635

636 **Figure 2.** Lidar observed nighttime hourly mean temperature composite in (a) spring, (b)

637 summer, (c) fall, and (d) winter.

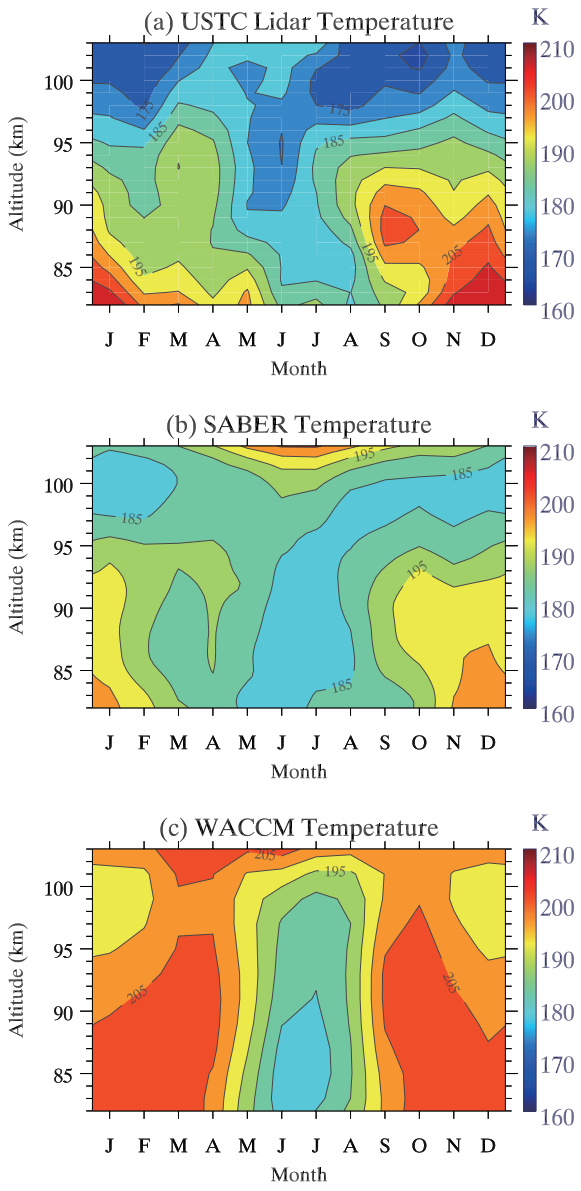

638

639 **Figure 3.** Monthly mean of mean temperature observed by (a) lidar, (b) SABER, and

640 simulated by (c) WACCM.

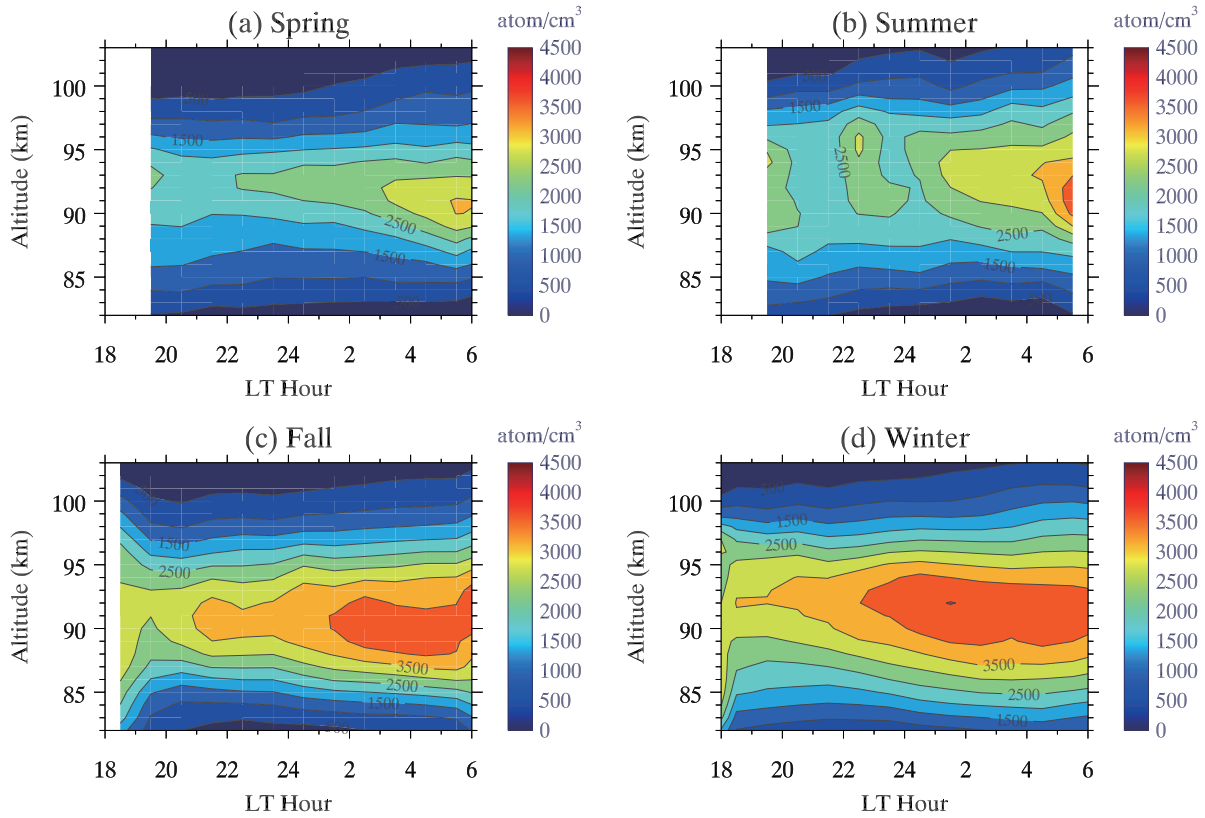

641

642 **Figure 4.** Same as Figure 2, but for sodium number density.

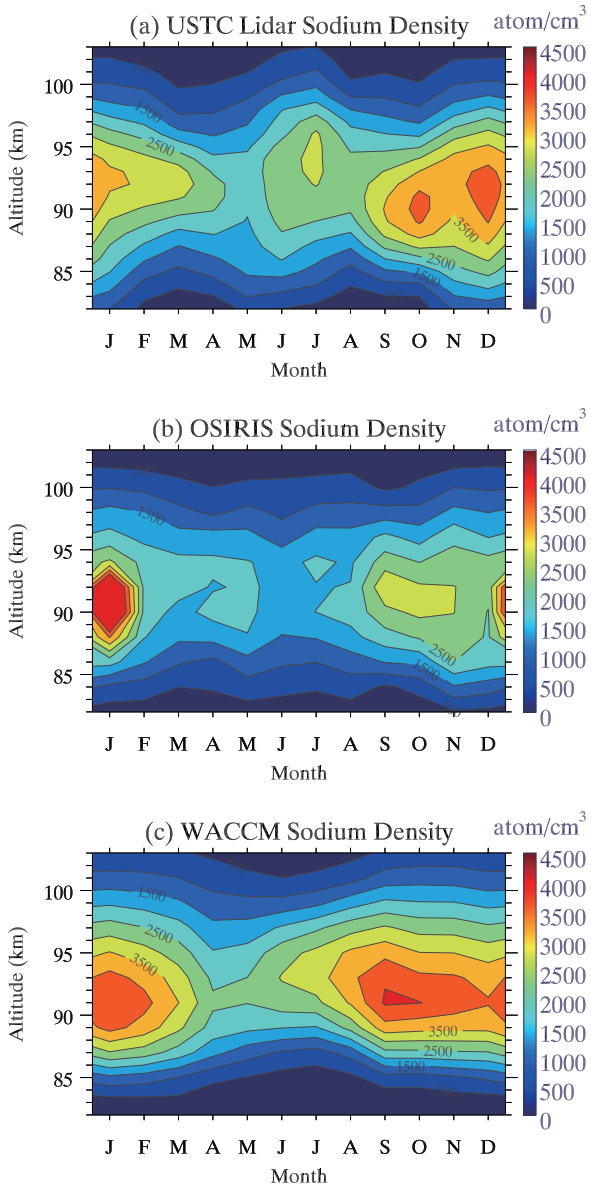

643

644 **Figure 5.** Monthly mean of nightly mean sodium density observed by (a) lidar and (b) Odin/

645 OSIRIS, and simulated by (c) WACCM.

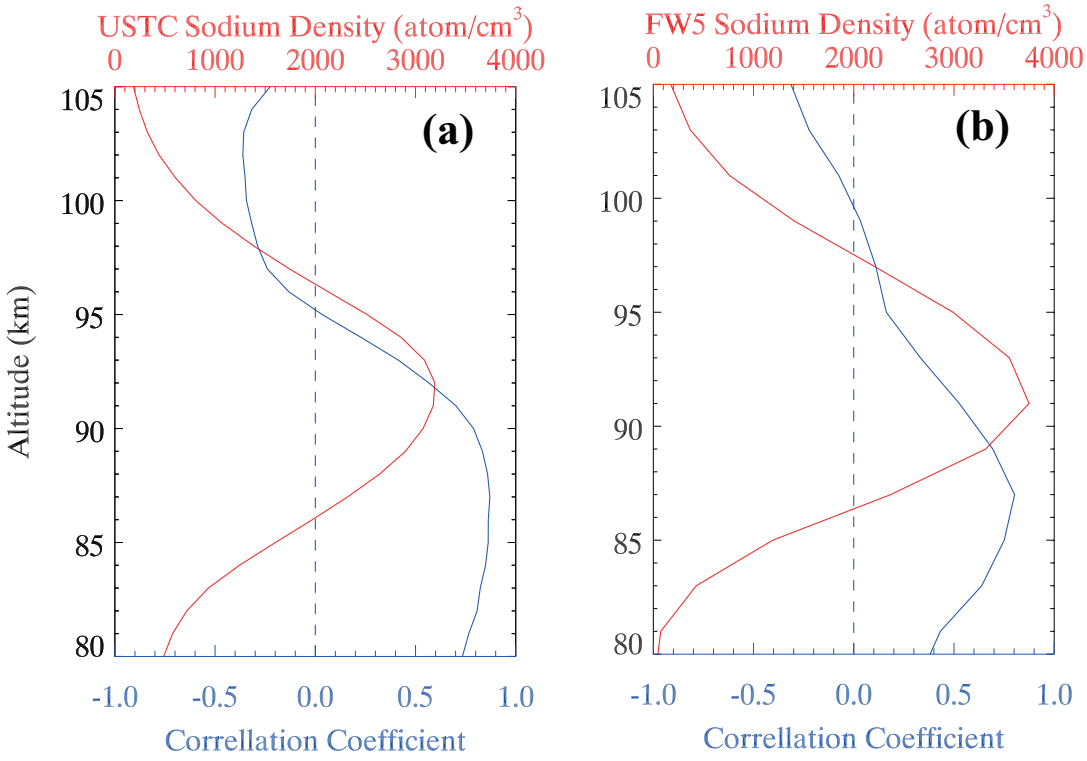

646

647 **Figure 6.** The vertical profiles of correlation coefficent (blue) between composite temperature

648 and relative sodium density perturbations, and annual mean sodium density (red), observed by

649 lidar (left) and simulated by WACCM (right).

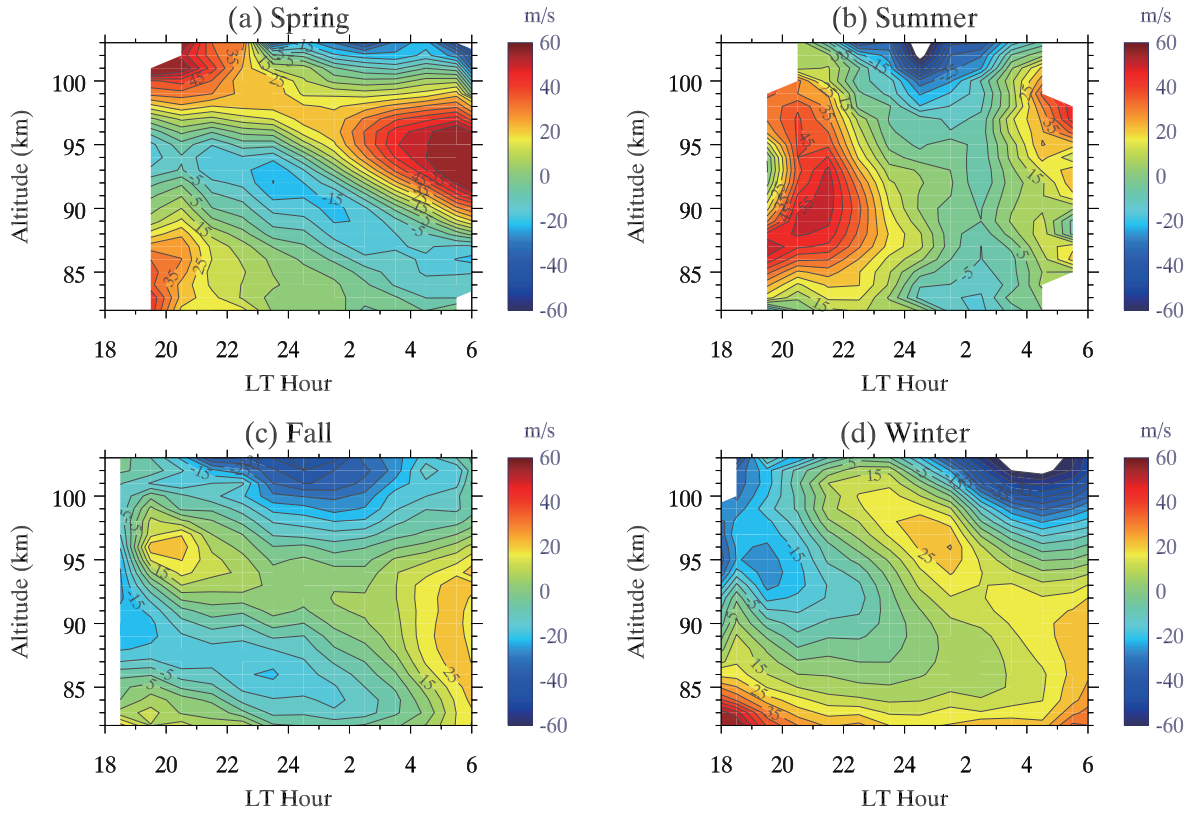

Figure 7. Same as Figure 2, but for zonal wind.

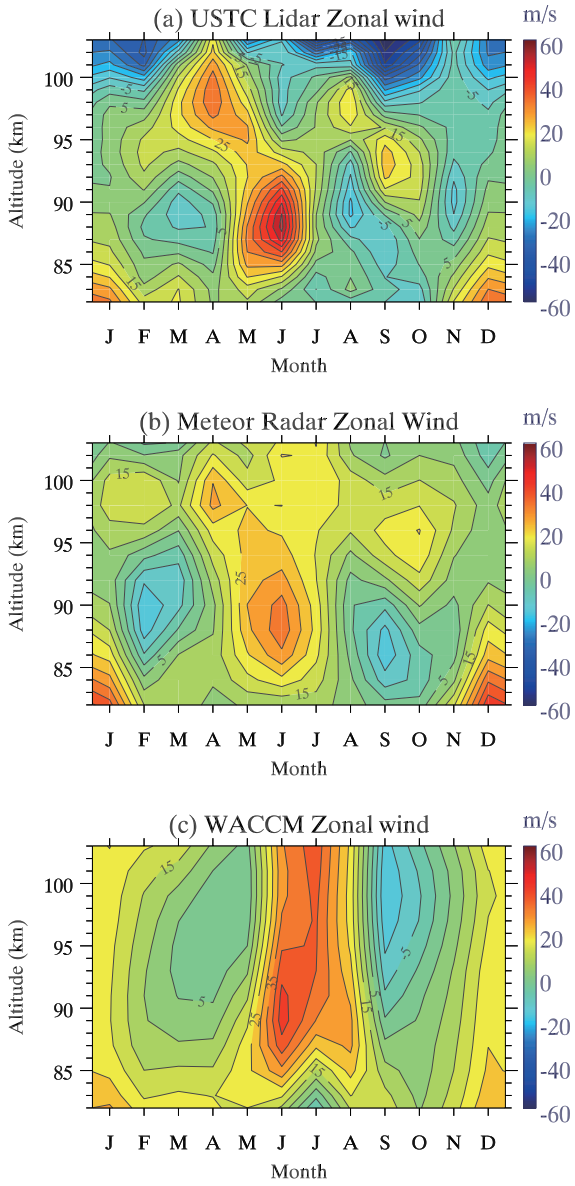

652

653 **Figure 8.** Monthly mean of nightly mean zonal wind observed by (a) lidar, (b) meteor radar,

654 and simulated by (c) WACCM.

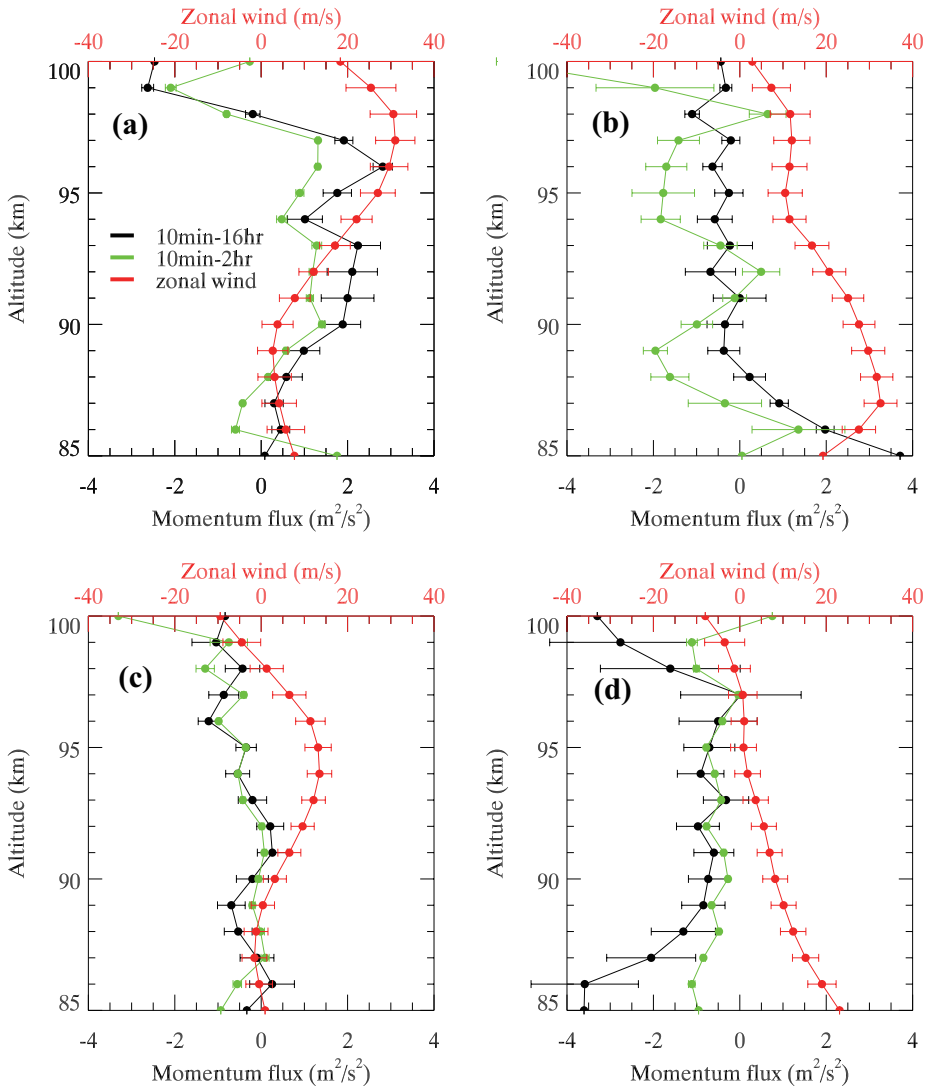

655

656 **Figure 9.** Comparision of seasonal mean of nightly mean zonal wind (red) and zonal
657 momentum flux for 10min - 16hr (blue) and 10min - 2hr (green) observed by lidar in (a)
658 spring, (b) summer, (c) fall, and (d) winter.